Science

AAAS

Terahertz Metamaterials for Linear Polarization Conversion and Anomalous Refraction

Nathaniel K. Grady *et al.*
Science **340**, 1304 (2013);
DOI: 10.1126/science.1235399

Terahertz Metamaterials for Linear Polarization Conversion and Anomalous Refraction

Nathaniel K. Grady,[1] Jane E. Heyes,[1] Dibakar Roy Chowdhury,[1] Yong Zeng,[2] Matthew T. Reiten,[1] Abul K. Azad,[1] Antoinette J. Taylor,[1] Diego A. R. Dalvit,[2] Hou-Tong Chen[1]*

Polarization is one of the basic properties of electromagnetic waves conveying valuable information in signal transmission and sensitive measurements. Conventional methods for advanced polarization control impose demanding requirements on material properties and attain only limited performance. We demonstrated ultrathin, broadband, and highly efficient metamaterial-based terahertz polarization converters that are capable of rotating a linear polarization state into its orthogonal one. On the basis of these results, we created metamaterial structures capable of realizing near-perfect anomalous refraction. Our work opens new opportunities for creating high-performance photonic devices and enables emergent metamaterial functionalities for applications in the technologically difficult terahertz-frequency regime.

Control and manipulation of electromagnetic (EM) polarization states has greatly affected our daily life, from consumer products to high-tech applications. Conventional state-of-the-art polarization converters use birefringence or total internal reflection effects (1) in crystals and polymers, which cause phase retardation between the two orthogonally polarized wave components. Expanding their typically limited bandwidth requires complex designs using multilayered films or Fresnel rhombs. At microwave and millimeter-wave frequencies, narrowband polarization converters have been constructed by using metallic structures, such as birefringent, multilayered meander-line gratings (2). Fabrication challenges and high losses render these unsuitable for optical frequencies (3).

Metamaterials have enabled the realization of many phenomena and functionalities unavailable through use of naturally occurring materials (4–6). Many basic metamaterial structures, such as metal split-ring resonators (7), exhibit birefringence suitable for polarization conversion (8–16), which has been mostly investigated in the microwave frequency range. Broadband metamaterial circular polarizers have been demonstrated in the

[1]Center for Integrated Nanotechnologies, MS K771, Los Alamos National Laboratory, Los Alamos, NM 87545, USA. [2]Theoretical Division, MS B213, Los Alamos National Laboratory, Los Alamos, NM 87545, USA.
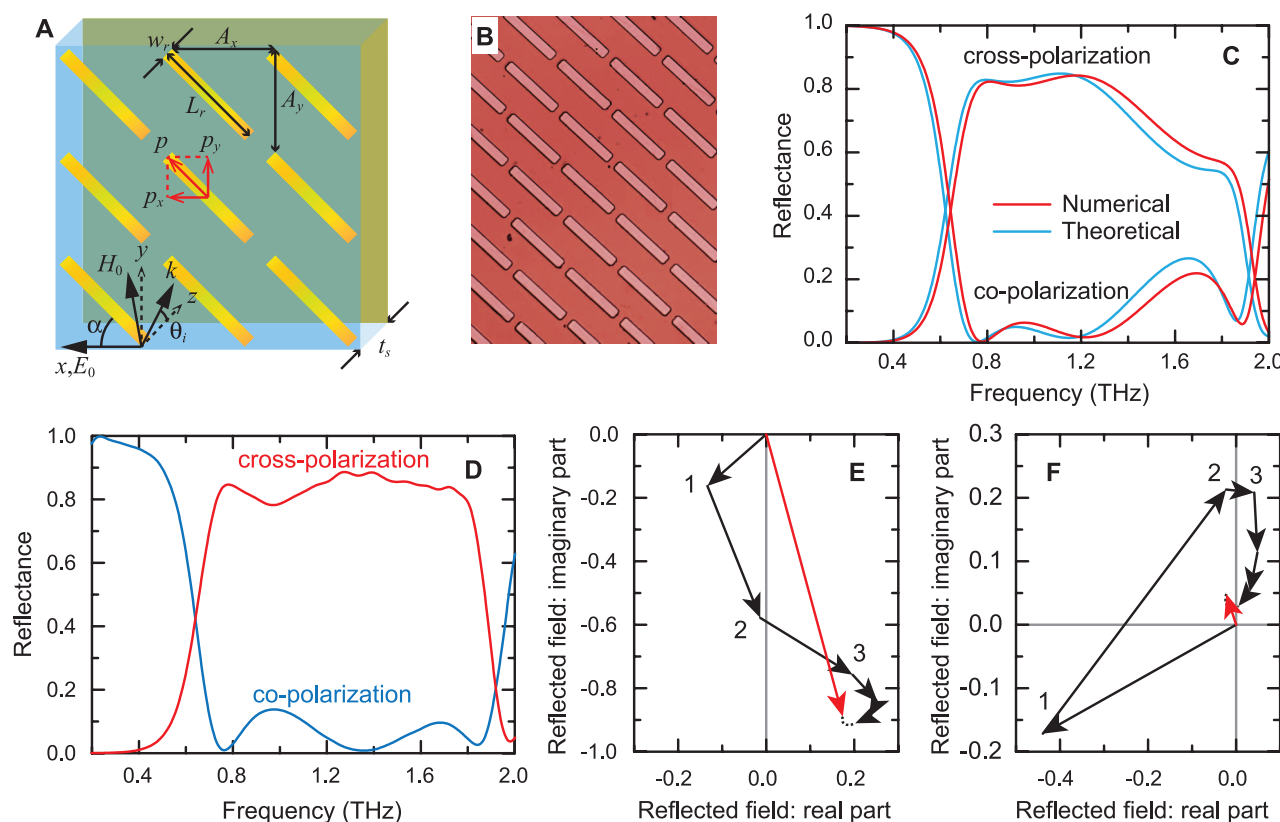
*Corresponding author. E-mail: chenht@lanl.gov

Fig. 1. Broadband polarization conversion in reflection. (**A**) Schematic and (**B**) optical micrograph of the metamaterial linear polarization converter. Both the gold cut-wire array and the gold ground plane are 200 nm thick, and they are separated by a polyimide dielectric spacer with thickness $t_s = 33$ μm and dielectric constant $\varepsilon = 3(1 + 0.05i)$. The periodicity $A_x = A_y = 68$ μm, cut-wire length $L_r = 82$ μm, and width $w_r = 10$ μm. The incidence angle $\theta_i = 25°$, and the incident electric field $\boldsymbol{E}_0$ is linearly polarized in the x direction (s-polarized), with an angle $\alpha = 45°$ with respect to the cut-wire orientation. (**C**) Numerically simulated and theoretically calculated, and (**D**) experimentally measured co- and cross-polarized reflectance. (**E**) Cross- and (**F**) copolarized multiple reflections theoretically calculated at 0.76 THz, revealing the constructive and destructive interferences, respectively. Similar behavior occurs for other frequencies as well. The numbers j (1, 2, and 3) indicate the ($j − 1$)-th roundtrip within the device. The red arrows are the converged cross- and copolarized reflected fields.

optical regime by using gold helix structures (*17*) and stacked nanorod arrays with a tailored rotational twist (*18*). Metamaterial-based polarimetric devices are particularly attractive in the terahertz frequency range due to the lack of suitable natural materials for terahertz device applications. However, the currently available designs suffer from either very limited bandwidth or high losses (*19–21*). In this work, we demonstrate high-efficiency and broadband, linear, terahertz polarization conversion using ultrathin planar metamaterials. In addition, our designs enable a dramatic improvement of the recently demonstrated anomalous (or generalized laws of) reflection/refraction (*22, 23*) by eliminating the ordinary components.

Our first metamaterial linear polarization converter design (Fig. 1, A and B) operates in reflection and consists of a metal cut-wire array and a metal ground plane separated by a dielectric spacer. We consider an incident wave E_0 linearly polarized in the *x* direction. It excites a dipolar oscillation *p* mainly along the cut-wires, which has parallel (p_x) and perpendicular (p_y) components to E_0. Whereas E_0 and p_x determine the co-polarized scattered field, p_y results in cross-polarized scattering, forming the dispersive reflection and
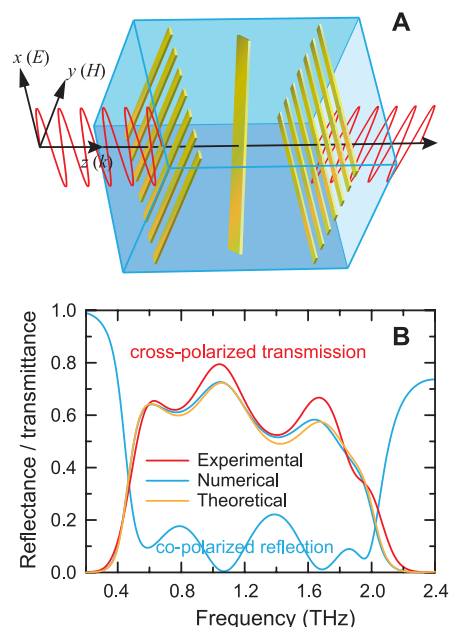

Fig. 2. Broadband polarization conversion in transmission. (**A**) Schematic of the unit cell of the metamaterial linear polarization converter, in which a normally incident *x*-polarized wave is converted into a *y*-polarized one. The cut-wire array is the same as in Fig. 1, the spacer is polyimide, and the separation between the cut-wire array and the gratings is 33 μm. The gold grating wire width is 4 μm, periodicity is 10 μm, and thickness is 200 nm. For this freestanding device, the gratings are covered with 4-μm-thick polyimide caps. (**B**) Cross-polarized transmittance obtained through experimental measurements, numerical simulations, and theoretical calculations. Also shown is the numerically simulated copolarized reflectance.

transmission (fig. S1) of the cut-wire array. Without the ground plane, the polarization conversion efficiency is low, and the overall reflection and transmission are elliptically polarized. The ground plane and the cut-wire array form a Fabry-Pérot–like cavity (*24, 25*); the consequent interference of polarization couplings in the multireflection process may either enhance or reduce the overall reflected fields with co- and cross-polarizations (*26*).

We validated this concept by performing full-wave numerical simulations (Fig. 1C) (the polarization angle dependence is available in fig. S2). Between 0.7 and 1.9 THz, the cross-polarized reflection carries more than 50% of the incident power, and the copolarized component is mostly below 20%. Between 0.8 and 1.36 THz, the cross-polarized reflection is higher than 80%, and the copolarized one is below 5%, representing a broadband and high-performance linear polarization converter in reflection. Further numerical simulations revealed that this broadband and high-efficiency performance is sustained over a wide incidence angle range (fig. S3). The broadband operation results from the superposition of multiple polarization conversion peaks around 0.8, 1.2, and 1.9 THz (Fig. 1C), at which the efficiency is mainly limited by dielectric loss. At other frequencies, the copolarized reflection also contributes.

Our fabricated devices are characterized by using terahertz time-domain spectroscopy (THz-TDS) (fig. S4), as detailed in (*26*). The experimental co- and cross-polarized reflectance (Fig. 1D) reproduces the linear polarization conversion seen in the numerical simulations. From 0.65 to 1.87 THz, the cross-polarized reflection relays more than 50% of the incident power and over 80% between 0.73 and 1.8 THz, with the highest conversion efficiency of 88% at 1.36 THz. The copolarized reflectance is mostly less than 14% and approaches zero at some frequencies, demonstrating the capability of rotating the input linear polarization by 90° with high output purity over a broad bandwidth.

The underlying reason for the enhanced polarization conversion is the interference between the multiple polarization couplings in the Fabry-Pérot–like cavity. To confirm this interpretation, we calculated the co- and cross-polarized reflected fields caused by each roundtrip within the cavity (fig. S5). For each individual reflection, we plotted the complex reflected field in Fig. 1, E and F. As expected, the superposition of these partial cross-polarized reflected fields results in a constructive interference and gives a near-unity overall cross-reflection (Fig. 1E, red arrow); the superposition of these partial copolarized reflected fields results in a destructive interference and gives a zero overall coreflection (Fig. 1F, red arrow). The calculated overall reflections (Fig. 1C) are in excellent agreement with both the numerical simulations and experimental data (*26*).

Many applications require linear polarization conversion in transmission mode, for which the metal ground plane must be replaced. Our solution is to use a metal grating that transmits the

cross-polarized waves while still acting as a ground plane for copolarized waves. To retain the backward-propagating cross-polarized waves without blocking the incident waves, we added an orthogonal metal grating in front of the cut-wire (Fig. 2A). In addition, we added a 4-μm-thick polyimide capping layer both before the front and behind the back grating. This ultrathin, freestanding device serves as a high-performance linear polarization converter in transmission with reduced co- and cross-polarized reflections. In Fig. 2B, we plotted the numerically simulated cross-polarized transmittance and copolarized reflectance, for normal incidence with an *x*-polarized incident electric field [this device also operates over a wide incidence angle range (fig. S6)]. Also shown in Fig. 2B are the theoretical multireflection model results (*26*) and measured data for our fabricated device. There is excellent agreement among the numerical, experimental, and theoretical results. The device is able to rotate the linear polarization by 90°, with a conversion efficiency exceeding 50% from 0.52 to 1.82 THz, with the highest efficiency of 80% at 1.04 THz. In both simulation and experiments, the copolarized transmission and cross-polarized reflection are practically zero because of the use of gratings. The measured ratio between the co- and cross-polarized transmittance is less than 0.1 between 0.2 and 2.2 THz, covering the whole frequency range in a typical THz-TDS. The device performance, limited by the dielectric loss and copolarized reflection (Fig. 2B), can be further improved through optimizing the structural design and using lower-loss dielectric materials.

Recent demonstrations of the general laws of reflection/refraction and wavefront-shaping (*22, 23*) rely on creating a phase gradient in the cross-polarized scattering from anisotropic metamaterials. However, the single-layered metamaterial only produced weak anomalously reflected/refracted beams, with most of the power remaining in the ordinary beams. Our high-efficiency linear polarization converters allow us to accomplish broadband, near-perfect anomalous reflection/refraction by largely eliminating the ordinary beams. We used eight anisotropic resonators with various geometries and dimensions in a super-unit-cell (Fig. 3, A and B) to create a linear phase variation of the cross-polarized transmission spanning a 2π range. The resonator dimensions were determined through numerical simulations and are specified in fig. S7. Each of these resonators can be used to construct a high-performance linear polarization converter with similar cross-polarized transmission but a phase increment of $\sim\pi/4$ (Fig. 3C). Therefore, when combined into the super-unit-cell shown in Fig. 3, A and B, we expect a linear phase gradient of the cross-polarized transmitted wavefront, resulting in anomalous refraction.

We characterize our fabricated free-standing sample under normal incidence ($\theta_i = 0$) (*26*). In Fig. 3D, we plotted the cross-polarized transmittance as a function of frequency and transmission angle (the measured co-polarized transmission is negligible). Over a broad bandwidth, the ordinary
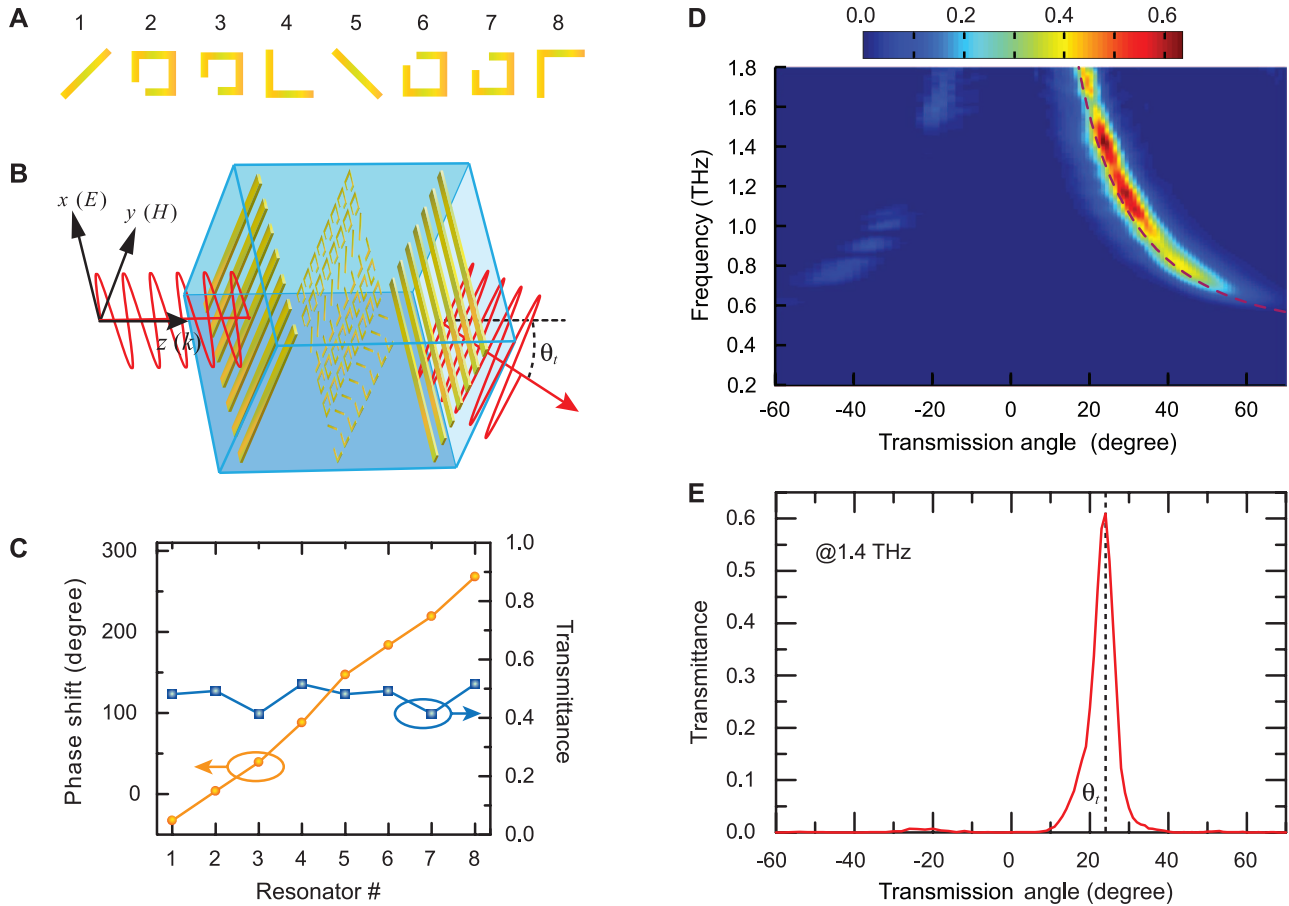
Fig. 3. Broadband and near-perfect anomalous refraction. (**A**) Resonator array super-unit-cell within the (**B**) anomalous refraction design (not to scale). A normally incident x-polarized wave is converted to a y-polarized transmission beam, which bends in the x-z plane to an angle θ_t with respect to the z axis. (**C**) The simulated cross-polarized transmittance and corresponding phase shift when each individual resonator is used in the linear polarization converter. (**D**) Experimentally measured cross-polarized transmittance as a function of frequency and angle. The dashed curve is the theoretically calculated frequency-dependent bending angle. (**E**) Cross-polarized transmittance at 1.4 THz under normal incidence as a function of angle.

refraction ($\theta_t = 0$) is practically zero, and only the anomalous beam is transmitted at a frequency-dependent refraction angle θ_t following the generalized law of refraction (22): $n_2\sin(\theta_t) - n_1\sin(\theta_i) = d\Phi/dx$, where $n_1 = n_2 = 1$ for the surrounding air, $d\Phi/dx = \lambda_0/D_1$ is the phase gradient imposed by the sample, λ_0 is the free space wavelength, and $D_1 = 560$ μm is the periodicity of the super-unit-cell along the phase gradient (x direction). The calculated frequency-dependent anomalous refraction angle is plotted as the dashed curve in Fig. 3D, revealing excellent agreement with the experimental results. At 1.4 THz ($\lambda_0 = 214$ μm), the angle-dependent transmittance (Fig. 3E) shows a maximum output power of 61% at $\theta_t = 24°$ and reveals minimal transmission at negative angles (0.6% at −24°). Also, the anomalous refraction intensity drops to zero as λ_0 approaches the periodicity D_1 corresponding to 0.54 THz, at which θ_t approaches 90° (Fig. 3D). This indicates that the incident wave is either totally reflected or converted to surface waves (27).

Our devices are ultrathin and operate within the technologically relevant terahertz frequency range, in which many important functionalities—including polarization conversion, beam steering, and wavefront shaping—have been extremely challenging to accomplish. Our results have shown that we can achieve broadband, high-performance linear polarization conversion and near-perfect anomalous refraction. Additional numerical simulations show that near-perfect anomalous reflection can also be accomplished by using the same concept (fig. S8). No particular optimization was undertaken to increase the conversion efficiency and bandwidth. Our demonstrations can be extended to other relevant frequencies. However, fabrication challenges and metal losses can become issues when approaching visible frequencies that substantially degrade the device performance. Our results form the foundation for more advanced applications; for instance, an appropriately constructed device can serve as a high-performance spatial light modulator. The wavefront shaping can result in a helical phase dependence forming Laguerre-Gauss modes carrying an orbital angular momentum that can acquire any integer value (28), which is useful in quantum entanglement (29) and enables opportunities in telecommunications (30).

References and Notes

1. M. Born, E. Wolf, *Principles of Optics* (Pergamon, Oxford, UK, ed. 6, 1980).
2. L. Young, L. A. Robinson, C. A. Hacking, *IEEE Trans. Antenn. Propag.* **21**, 376 (1973).
3. J. S. Tharp, B. A. Lail, B. A. Munk, G. D. Boreman, *IEEE Trans. Antenn. Propag.* **55**, 2983 (2007).
4. D. R. Smith, W. J. Padilla, D. C. Vier, S. C. Nemat-Nasser, S. Schultz, *Phys. Rev. Lett.* **84**, 4184 (2000).
5. J. B. Pendry, *Phys. Rev. Lett.* **85**, 3966 (2000).
6. D. Schurig et al., *Science* **314**, 977 (2006).
7. J. B. Pendry, A. J. Holden, D. J. Robbins, W. J. Stewart, *IEEE Trans. Microw. Theory Tech.* **47**, 2075 (1999).
8. J. M. Hao et al., *Phys. Rev. Lett.* **99**, 063908 (2007).
9. J. Y. Chin, M. Z. Lu, T. J. Cui, *Appl. Phys. Lett.* **93**, 251903 (2008).
10. M. Euler, V. Fusco, R. Cahill, R. Dickie, *IET Microw. Antenn. Propagat.* **4**, 1764 (2010).
11. Y. Q. Ye, S. He, *Appl. Phys. Lett.* **96**, 203501 (2010).
12. C. Menzel et al., *Phys. Rev. Lett.* **104**, 253902 (2010).
13. N. I. Zheludev, E. Plum, V. A. Fedotov, *Appl. Phys. Lett.* **99**, 171915 (2011).
14. Z. Y. Wei, Y. Cao, Y. C. Fan, X. Yu, H. Q. Li, *Appl. Phys. Lett.* **99**, 221907 (2011).
15. W. J. Sun, Q. He, J. M. Hao, L. Zhou, *Opt. Lett.* **36**, 927 (2011).
16. M. Mutlu, A. E. Akosman, A. E. Serebryannikov, E. Ozbay, *Phys. Rev. Lett.* **108**, 213905 (2012).
17. J. K. Gansel et al., *Science* **325**, 1513 (2009).
18. Y. Zhao, M. A. Belkin, A. Alu, *Nature Commun.* **3**, 870 (2012).

19. X. G. Peralta *et al.*, *Opt. Express* **17**, 773 (2009).
20. A. C. Strikwerda *et al.*, *Opt. Express* **17**, 136 (2009).
21. Y. J. Chiang, T. J. Yen, *Appl. Phys. Lett.* **102**, 011129 (2013).
22. N. F. Yu *et al.*, *Science* **334**, 333 (2011).
23. X. J. Ni, N. K. Emani, A. V. Kildishev, A. Boltasseva, V. M. Shalaev, *Science* **335**, 427 (2012).
24. H.-T. Chen *et al.*, *Phys. Rev. Lett.* **105**, 073901 (2010).
25. H.-T. Chen, *Opt. Express* **20**, 7165 (2012).
26. Materials and methods are available as supplementary materials on *Science* Online.
27. S. L. Sun *et al.*, *Nat. Mater.* **11**, 426 (2012).
28. S. Franke-Arnold, L. Allen, M. Padgett, *Laser Photon. Rev.* **2**, 299 (2008).
29. R. Fickler *et al.*, *Science* **338**, 640 (2012).
30. J. Wang *et al.*, *Nat. Photonics* **6**, 488 (2012).

Short-Range Quantum Magnetism of Ultracold Fermions in an Optical Lattice

Daniel Greif,[1] Thomas Uehlinger,[1] Gregor Jotzu,[1] Leticia Tarruell,[1,2]* Tilman Esslinger[1]†

Quantum magnetism originates from the exchange coupling between quantum mechanical spins. Here, we report on the observation of nearest-neighbor magnetic correlations emerging in the many-body state of a thermalized Fermi gas in an optical lattice. The key to obtaining short-range magnetic order is a local redistribution of entropy, which allows temperatures below the exchange energy for a subset of lattice bonds. When loading a repulsively interacting gas into either dimerized or anisotropic simple cubic configurations of a tunable-geometry lattice, we observe an excess of singlets as compared with triplets consisting of two opposite spins. For the anisotropic lattice, the transverse spin correlator reveals antiferromagnetic correlations along one spatial axis. Our work facilitates addressing open problems in quantum magnetism through the use of quantum simulation.

Quantum magnetism describes quantum many-body states of spins coupled by exchange interactions and lies at the heart of many fundamental phenomena in condensed matter physics (*1*, *2*). Spin systems often tend to show long-range order at low temperatures; however, the interplay of exchange interactions with geometry and quantum fluctuations can lead to quantum states characterized by their short-range magnetic order. Examples include valence-bond crystals, spin-liquids, and possibly high-temperature superconductors (*1–5*). Interestingly, the underlying many-body physics gives rise to computationally and theoretically intractable regimes, even in the phase diagrams of simple models such as the Fermi-Hubbard model. Moreover, the direct measurement of local spin correlations in solids remains a major challenge.

The controlled setting of ultracold fermionic atoms in optical lattices is regarded as a promising route to gain new insights into phases driven by quantum magnetism (*6–8*). This approach offers experimental access to a clean and highly flexible Fermi-Hubbard model with a distinct set of observables (*9*). For repulsively interacting fermions, density ordering in the metal–Mott insulator transition has been explored experimentally (*10*, *11*). Yet, progress toward entering the regime of quantum magnetism has been hindered by the ultralow temperatures and entropies required to observe exchange-driven spin ordering in optical lattices. For bosonic systems, promising progress has been reported: By mapping the spin onto the site occupation or the local phase of a Bose-Einstein condensate, the physics of one-dimensional (1D) decoupled Ising spin chains (*12*) and classical magnetism on a triangular lattice could be simulated (*13*). Furthermore, arrays of isolated double wells and plaquettes were used to study the exchange dynamics of artificially prepared few-boson systems (*14*, *15*).

To enable the study of quantum magnetic phenomena in thermalized many-body Hubbard systems, cooling schemes based on the redistribution of entropy between different regions of the trap have been suggested (*16*, *17*). In this work, we propose and implement a local entropy-redistribution scheme within the lattice structure to reach the regime of quantum magnetism. The atoms are either prepared in a dimerized or an anisotropic simple cubic lattice (Fig. 1). In both geometries, a subset of links of the underlying simple cubic lattice is set to a larger exchange energy as compared with the other links. As a result, the entropy is predominantly stored in configurations involving the weak links. For fixed total entropy in the trapped system, this allows us to reach temperatures between the two exchange-energy scales.

The experiment is performed with a harmonically confined, balanced two-component mixture of a quantum degenerate Fermi gas of ^{40}K. The atoms are prepared in two magnetic sublevels, $m_F = -9/2$ and $-7/2$, of the $F = 9/2$ hyperfine manifold, denoted by ↑ and ↓, at temperatures below 10% of the Fermi temperature. We load 50,000 to 100,000 repulsively interacting atoms at an s-wave scattering length of $106(1)a_0$ into the 3D optical lattice, where a_0 denotes the Bohr radius. The lattice is created by a combination of interfering laser beams

Fig. 1. Magnetic spin correlations. Schematic view of the nearest-neighbor spin correlations observed in the experiment. A two-component mixture of fermionic atoms (red and blue) is prepared close to half-filling in a cubic lattice with two different tunnel-coupling configurations. (**A**) Dimerized lattice with the strong dimer links t_d and weaker links t. Low temperatures lead to an excess number of singlets over triplets. (**B**) Anisotropic lattice with strong and weak tunneling t_s and t along different spatial axes. Antiferromagnetic spin correlations in the transverse direction are formed along the strong-link direction. In both panels, exemplary thermal excitations in the form of spin excitations, or holes, are shown.

Dimerized cubic lattice

Anisotropic cubic lattice

Singlet · Triplet · Antiferromagnetic spin correlation
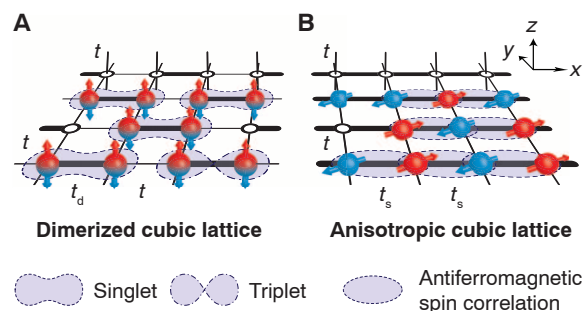
[1]Institute for Quantum Electronics, ETH Zurich, 8093 Zurich, Switzerland. [2]LP2N UMR 5298, Université Bordeaux 1, Institut d'Optique and CNRS, 351 Cours de la Libération, 33405 Talence, France.

*Present address: Institut de Ciencies Fotoniques, Mediterranean Technology Park, 08860 Castelldefels, Barcelona, Spain.
†Corresponding author. E-mail: esslinger@phys.ethz.ch